Theoretical and experimental study of second harmonic generation from the surface of the topological insulator Bi_2Se_3

J. W. McIver,[1,2] D. Hsieh,[1] S. G. Drapcho,[1] D. H. Torchinsky,[1] D. R. Gardner,[1] Y. S. Lee,[1] and N. Gedik[1,*]

[1]*Department of Physics, Massachusetts Institute of Technology, Cambridge, Massachusetts 02139, USA*

[2]*Department of Physics, Harvard University, Cambridge, Massachusetts 02138, USA*

(Received 23 April 2012; revised manuscript received 28 June 2012; published 27 July 2012)

We develop a theoretical model that describes the second harmonic generation of light from the surface of the topological insulator Bi_2Se_3 and experimentally demonstrate that the technique is sensitive to the surface electrons. By performing a crystal symmetry analysis of $Bi_2Se_3(111)$ we determine the nonlinear electric susceptibility tensor elements that give rise to second harmonic generation. Using these results, we present a phenomenological model that shows that the relative magnitudes of these tensor elements can be determined by measuring the polarization and intensity of the radiated second harmonic light as a function of the in-plane crystal orientation and incident laser polarization. We describe optical techniques capable of isolating second harmonic light and, using these techniques, we measure the first-order linear optical and second-order nonlinear optical responses as a function of crystal orientation and laser polarization on bulk single crystals of $Bi_2Se_3(111)$. The experimental results are consistent with our theoretical description. By comparing the data to our theoretical model we determine that a portion of the measured second harmonic light originates from the accumulation region of $Bi_2Se_3(111)$, which we confirm by performing surface doping-dependent studies. Our results show that second harmonic generation is a promising tool for spectroscopic studies of topological surfaces and buried interfaces.

DOI: 10.1103/PhysRevB.86.035327 PACS number(s): 78.20.Ci, 78.68.+m, 03.65.Vf, 71.70.Ej

I. INTRODUCTION

The three-dimensional (3D) topological insulator[1–3] is a new quantum phase of matter that is characterized by an inverted bulk band gap and topologically protected surface states,[4,5] which have been comprehensively imaged by both photoemission[4–8] and tunneling[9,10] spectroscopies. The electrical response properties of an isolated surface are predicted to be highly novel, including protection against backscattering from nonmagnetic impurities[1–3] and a switchable spin-polarized electrical current.[11–13] When interfaced with certain topologically trivial materials, the surface states are predicted to evolve into new broken-symmetry electronic phases that may exhibit topological superconductivity[2] and an anomalous half-integer quantum Hall effect;[2,14] they have been proposed as media to search for Majorana fermions[1,2] and charge fractionalization in three dimensions.[15] Owing to these exciting theoretical proposals, the recent discovery of 3D topological insulator phases in $Bi_{1-x}Sb_x$,[4,5] Bi_2Se_3,[6,16] and related materials[7,16,17] has generated great interest to measure their symmetry and electrical properties at an isolated surface or buried interface. However, a major experimental obstacle has been the high density of mobile electrons in the bulk of these materials, which can overwhelm the surface or interface electrical responses. Although transport results on electrically gated samples show evidence of surface carrier modulation,[18–20] the contributions to the electrical response from carriers on different surfaces and in the bulk are difficult to separate and require highly insulating samples. Moreover, contacts and gates deposited on the surface may perturb the intrinsic surface electronic structure.[21]

Optical probes have been proposed as a contact-free alternative that can be focused onto a single surface.[11,14,22,23] However, most experiments to date have been limited to the linear optical regime, which has been shown to be dominated by the bulk electrical response[24–26] except in the limit of very thin samples.[27,28] Recently, nonlinear second harmonic generation (SHG) of light from bulk single crystals of Bi_2Se_3 was shown to be highly sensitive to electrons confined to the surface and accumulation region.[29,30] The underlying principle for this surface sensitivity is that SHG is predominantly generated where inversion symmetry is broken,[31] which only occurs at the surface of the bulk inversion-symmetric Bi_2Se_3 and in the accumulation region, where the band-bending-induced electric field breaks the inversion symmetry.

In this work, we develop a theoretical model that describes the SHG intensity from Bi_2Se_3 in terms of the second- and third-order nonlinear electric susceptibilities. By performing a symmetry analysis of Bi_2Se_3 we identify the susceptibility tensor elements that contribute to SHG and show that their relative magnitudes can be determined by measuring the intensity and polarization of the emitted SHG as a function of crystal orientation and incident laser polarization. To test the model, bulk single crystals of Bi_2Se_3 were grown and characterized and SHG experiments were performed using both linear and circularly polarized laser light. The experimental results are described well by our theoretical model. Application of the model to our data shows that approximately half of the SHG from Bi_2Se_3 at long times after cleaving in air originates from the surface, while the rest originates from the accumulation region. A surface doping-dependent study verifies that the SHG intensity depends on the surface carrier concentration, which shows that SHG can be used to optically probe changes in the surface Fermi level.

The paper is organized as follows: In Sec. II, we perform a crystal symmetry analysis on Bi_2Se_3 to determine the nonlinear susceptibility tensor elements that give rise to SHG. We then present a phenomenological model that describes how these tensor elements are manifested in the SHG intensity and polarization. In Sec. III, we first detail the SHG growth procedures, sample characterization results,

and SHG experimental methods used to isolate the surface response. We then report the measured SHG intensity and polarization and compare the results to the theoretical model developed in Sec. II. Finally, we report the effects of surface doping on SHG and investigate circular dichroism (CD) SHG. A summary is provided in Sec. IV, followed by the Appendix.

II. THEORETICAL BACKGROUND

This section is organized in two parts. In Sec. II A, we determine the susceptibility tensor elements that give rise to SHG in Bi_2Se_3 by performing a crystal symmetry analysis. In Sec. II B, we present a phenomenological model that describes the intensity and polarization of second harmonic light generated from Bi_2Se_3 using these tensor elements.

A. Symmetry analysis and electric susceptibility tensors of Bi_2Se_3(111)

The electrical response of a material is described by susceptibility tensors $\chi^{(n)}$ that relate the electric polarization of the material $\vec{P}$ to the applied electric field $\vec{E}$ through the power-series expansion[31]

$$P_i = \chi^{(1)}_{ij} E_j + \chi^{(2)}_{ijk} E_j E_k + \chi^{(3)}_{ijkl} E_j E_k E_l + \ldots, \qquad (1)$$

where the indices run through spatial coordinates. The susceptibility tensor elements of each $\chi^{(n)}$ can be determined by performing a crystal symmetry analysis. The bulk crystal structure of Bi_2Se_3(111), which belongs to space group D^5_{3d}, remains invariant under a group of symmetry operations T. These consist of (i) rotation along the (111) axis by 0°, 120°, and 240°; (ii) mirror reflection under planes a, b, and c (Fig. 1); and (iii) inversion symmetry about some center of inversion. Because $\chi^{(n)}$ must obey the same symmetries as the crystal, they must be invariant under the same group of symmetry

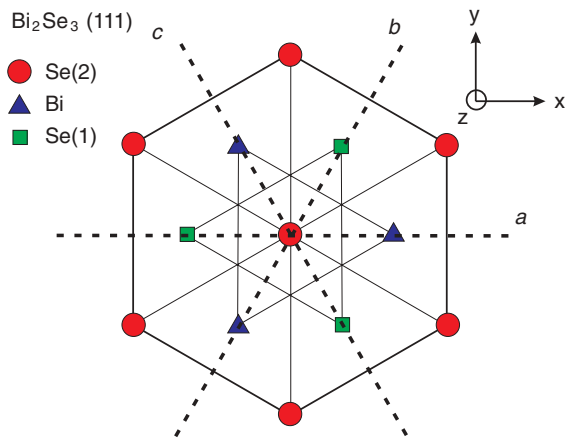

FIG. 1. (Color online) Schematic of the Bi_2Se_3 crystal coordinate system showing the C_{3v} symmetry of the (111) cleaved surface. The bulk D^5_{3d} symmetry is given by the addition of inversion symmetry. The threefold rotation symmetry and the three planes of mirror symmetry (a, b, and c) are illustrated. The topmost, second, and third atomic layers are Se(2), Bi, and Se(1), respectively. The beam coordinate system is shown at the top right.

operations that bring $\chi^{(n)}$ to $\chi^{(n)'}$, which is given by[31]

$$\chi^{(n)'}_{i_1 i_2 \ldots i_{n+1}} = \sum_{j_1, j_2 \cdots j_{n+1}} T_{i_1 j_1} T_{i_2 j_2} \ldots T_{i_{n+1} j_{n+1}} \chi^{(n)}_{j_1 j_2 \ldots j_{n+1}}. \qquad (2)$$

Under such transformations, the crystal symmetry greatly reduces the number of nonzero independent components of $\chi^{(n)}$.

We first examine the first-order response characterized by $\chi^{(1)}$ in Eq. (1). Because $\chi^{(1)}$ is an even-rank tensor and P_i and E_j are both odd under the operation of inversion, a first-order response is permitted regardless of whether or not crystal inversion symmetry is present. Therefore, the linear optical response can include contributions from both the inversion symmetric bulk of Bi_2Se_3 and the (111) surface, where inversion symmetry is necessarily broken.[31] The individual tensor elements can be found by transforming $\chi^{(1)}$ under the rotation, mirror, and inversion symmetry operations that characterize bulk Bi_2Se_3 via Eq. (2) and equating the resulting tensors. Using this procedure, we find that $\chi^{(1)}$ assumes the form

$$\chi^{(1)} = \begin{pmatrix} \chi^{(1)}_{11} & 0 & 0 \\ 0 & \chi^{(1)}_{22} & 0 \\ 0 & 0 & \chi^{(1)}_{33} \end{pmatrix}, \qquad (3)$$

where $\chi^{(1)}_{11} = \chi^{(1)}_{22}$, and $\chi^{(1)}_{33}$ are scalars.[32] This yields an isotropic first-order electrical response in the (111) plane. Although both bulk and surface contribute to this response, the bulk contribution usually dominates. This is because the linear optical response is an integrated measure over the depth to which light penetrates into the sample, which is typically of the order of hundreds of atomic layers.

We now analyze how the Bi_2Se_3(111) crystal symmetry affects the second-order dipolar response $\chi^{(2)}$. From Eq. (2) we see that all of the components of odd-rank tensors must vanish under the inversion operator $T_{ij} = -\delta_{ij}$ because each component is mapped to the negative of itself. Therefore, all 27 components of $\chi^{(2)}$ must be 0 in the inversion-symmetric bulk of Bi_2Se_3. However, at the cleaved (111) surface, inversion symmetry is broken and the crystal symmetry is reduced to C_{3v} symmetry. In the case of Bi_2Se_3, cleavage occurs naturally between two Se layers that are van der Waals bonded to expose large areas that are Se terminated.[1–3] Owing to this lack of inversion symmetry at the surface, nonvanishing components of odd-rank tensors such as $\chi^{(2)}$ are permitted to exist. The individual $\chi^{(2)}$ tensor components for Bi_2Se_3 are reported in the Appendix. In Sec. II B we show how these tensor elements are manifested in the SHG intensity and polarization as a function of the crystal orientation and incident laser polarization.

In addition to the surface $\chi^{(2)}$ contribution, SHG can be generated by accumulation layer electrons. These are bulk electrons confined near the surface by a band-bending-induced electric field $\vec{\mathcal{E}}$ directed perpendicular to the surface. SHG is highly sensitive to a static electric field because it acts to break inversion symmetry over the accumulation region (Fig. 2). Electric-field-induced SHG is commonly observed in the context of metal-electrolyte interfaces[33] and is theoretically described by a third-order process, $P_i(2\omega) = \chi^{(3)}_{ijkl} \mathcal{E}_j(\omega) E_k(\omega) E_l(0)$, that acts in addition to $\chi^{(2)}$.[31,33,34] Because $\chi^{(3)}$ has the same symmetry constraints as $\chi^{(2)}$, the

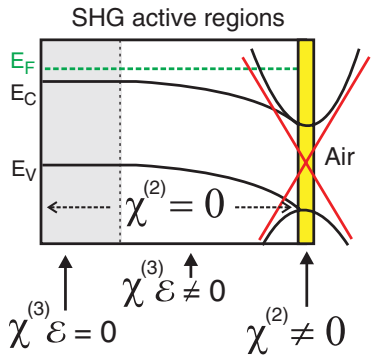

FIG. 2. (Color online) Schematic of the energy evolution of the bulk conduction band minimum (E_C) and bulk valence band maximum (E_V) relative to the Fermi level (E_F) as a function of distance to the air covered surface. The SHG active regions are where $\chi^{(2)} + \chi^{(3)}\mathcal{E} \neq 0$, which represent the surface (yellow) and accumulation-region (white) contributions respectively.

overall symmetry of the SHG intensity as a function of the crystal orientation must remain unchanged in the presence of $\vec{\mathcal{E}}$, with each $\chi^{(2)}$ tensor element simply being enhanced by the addition of a $\chi^{(3)}\vec{\mathcal{E}}$ tensor element. The nonvanishing $\chi^{(3)}$ tensor elements for Bi_2Se_3 are determined in the Appendix.

We note that there may also be higher multipole bulk contributions to SHG that can be finite even in inversion-symmetric systems[31] and that will have the same symmetry properties as both the surface $\chi^{(2)}$ and $\chi^{(3)}$ tensors[32] shown above. The bulk electric quadrupole and magnetic dipole contributions are the dominant of these higher multipole susceptibilities, however, they are generally suppressed relative to the dipolar susceptibilities by a factor of ka, where k is the wave vector of the incident light and a is a lattice constant.[31] In reflection measurements, the bulk contribution only comes from a layer within the optical penetration depth (ξ) of the incident light, which we determine to be ~25 nm at 795 nm (Sec. III A). The surface contribution will come from the entire depth d over which the surface wave functions penetrate into the bulk, which is of the order $d \equiv \hbar v_f/\Delta \sim 10$ Å for states within the bulk gap and is much larger for states not in the bulk gap, where v_f is the Fermi velocity, $\hbar$ is the reduced Planck's constant, and Δ is the bulk band-gap energy. Therefore, the relative intensity of the surface to bulk second harmonic radiation is approximately $|\frac{1}{ka}\frac{d}{\xi}|^2 = |\frac{7.95\times10^3\,\text{Å}}{2\pi\times2\,\text{Å}}\frac{10\,\text{Å}}{2.5\times10^2\,\text{Å}}|^2 \sim 640$. Indeed, measurements on other strong spin-orbit coupled materials, such as Au, in the regime where interband transitions dominate ($\Delta < \hbar\omega$) have shown that these bulk contributions are greatly suppressed.[35] Bulk contributions have only been shown to be observable when $\Delta > \hbar\omega$, where the penetration depth of the light into the crystal is very deep.[36] All of our measurements were performed in the regime $\Delta < \hbar\omega$ and we experimentally demonstrate in Sec. III C, by varying the surface carrier density, that these higher order bulk effects are indeed not dominant.

B. Phenomenological model of surface SHG

In this section, we show how the intensity of second harmonic radiation is related to the nonlinear susceptibility tensors derived in Sec. II A. Our phenomenological model of surface SHG follows the convention developed by Mizrahi and Sipe,[37] which builds on the earlier work of Heinz[38] and Bloembergen and Pershan.[39] The model assumes that the source of surface SHG is a thin electric dipole sheet confined to the surface. Following the notation used in Ref. 37 for surface SHG from a thick crystal in the reflection geometry, the second harmonic intensity $I(2\omega)$ is given by

$$I(2\omega) = A \times |\hat{e}_i(2\omega)\,(\chi_s)_{ijk}\,\hat{e}_j(\omega)\hat{e}_k(\omega)|^2 I(\omega)^2, \qquad (4)$$

where A is a geometrical constant, $\hat{e}(\omega)$ is the beam polarization of the incoming radiation field inside the crystal, $\hat{e}(2\omega)$ is the beam polarization of the outgoing second harmonic radiation field inside the crystal, $I(\omega)$ is the intensity of the incident beam, χ_s is the complex surface nonlinear susceptibility tensor, and the indices run through x, y, and z. The polarization directions are defined in Fig. 3. The incident unit polarization vector is given by

$$\hat{\mathbf{e}}(\omega) = \frac{E^s_{\text{in}}}{|E_{\text{in}}|}t^s_{0m}\hat{s} + \frac{E^p_{\text{in}}}{|E_{\text{in}}|}t^p_{0m}\hat{p}_-, \qquad (5)$$

where $E^{s,p}_{\text{in}}$ are the s- and p-polarized components of the incident electric field, $t^{s,p}_{0m}$ are the complex Fresnel coefficients for transmission of the fundamental beam from air into the medium with electric permittivity ϵ, and $\hat{s}$ and $\hat{p}_-$ are the s- and p-polarization directions of the fundamental beam in the crystal. The outgoing second harmonic unit polarization vector is given by

$$\hat{\mathbf{e}}(2\omega) = \frac{E^S_{\text{out}}}{|E_{\text{out}}|}(1 + R^s_{0m})\hat{S} + \frac{E^P_{\text{out}}}{|E_{\text{out}}|}(\hat{P}_{0+} + R^p_{0m}\hat{P}_{0-}), \qquad (6)$$

where $E^{S,P}_{\text{out}}$ are the s- and p-polarized components of the outgoing second harmonic electric field, $R^{s,p}_{0m}$ is the complex Fresnel coefficient for reflection of the second harmonic beam off the bulk medium beneath the surface electric dipole sheet,[37]

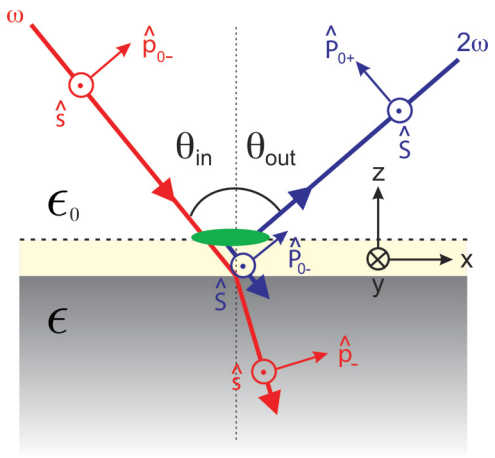

FIG. 3. (Color online) Schematic of the incoming and outgoing laser-beam geometry and polarizations. Polarization vectors of the fundamental and second harmonic beams are labeled by lowercase and uppercase letters, respectively. The cream-colored region at $z = 0$ denotes the electric dipole sheet at the surface as described in Ref. 37. The interaction volume of the beams is demarcated by the filled (green) oval region. The refracted fundamental beam is displaced downward and the fundamental and second harmonic beams are separated for visual clarity.

$\hat{S}$ denotes the s-polarized direction of the reflected second harmonic light, $\hat{P}_{0+}$ is the p-polarized component of second harmonic light that is reflected off the top surface of the dipole sheet, and $\hat{P}_{0-}$ is the p-polarized component that reflects off the bulk medium after being generated at the surface.

In our model we assume that $(\chi_s)_{ijk} = \chi^{(2)}_{ijk} + \chi^{(3)}_{ijkl}\mathcal{E}_l$ in Eq.(4), which represents the combined surface plus accumulation-region response. This is a simplification, as the presence of a band-bending-induced electric field $\mathcal{E}$ will alter the index of refraction, and hence the Fresnel coefficients, as a function of depth into the bulk. However, accounting for this effect is beyond the scope of our work. In our calculation we let $\vec{\mathcal{E}}$ lie only along the z direction because the atomic layers must be equipotentials. The Fresnel coefficients at the fundamental and second harmonic frequency were calculated using the Fresnel equations,[40] where, for the complex indices of refraction $\tilde{n} = n + ik$, we use $\tilde{n}(\omega) = 5.46 + i2.57$ and $\tilde{n}(2\omega) = 2.07 + i3.43$, which we determine experimentally for our Bi_2Se_3 samples in Sec. III A. We assume that $\theta_{\text{in}} = \theta_{\text{out}} = 45^\circ$ based on our experimental configuration (Sec. III A). Using these parameters in Eqs. (4)–(6), we obtain expressions for the intensity of second harmonic radiation as a function of the in-plane crystal orientation angle ϕ (Fig. 1) under different linear polarization geometries and circular polarization geometries as follows:

$$\begin{aligned}
I_{PP}(2\omega) &= B|(0.0012 + 0.0034i)c^{(3)} + (0.076 - 0.038i)c^{(2)} \\
&\quad + (0.00030 - 0.0012i)c^{(4)} \\
&\quad - (0.0030 - 0.030i)c^{(1)}\cos(3\phi)|^2, \\
I_{SP}(2\omega) &= B|(0.045 - 0.027i)c^{(2)} \\
&\quad + (0.00013 - 0.018i)c^{(1)}\cos(3\phi)|^2 \\
I_{SS}(2\omega) &= B|(0.0019 + 0.014i)c^{(1)}\sin(3\phi)|^2 \\
I_{PS}(2\omega) &= B|(-0.00092 - 0.024i)c^{(1)}\sin(3\phi)|^2
\end{aligned} \tag{7}$$

and

$$\begin{aligned}
I_{RS}(2\omega) &= B\,|(0.0019 - 0.0011i)\,c^{(3)} \\
&\quad - (0.037 - 0.0031i)\,c^{(1)}\cos(3\phi) \\
&\quad + (0.0028 + 0.0378i)\,c^{(1)}\sin(3\phi)|^2, \\
I_{LS}(2\omega) &= B\,|(0.0019 - 0.0011i)\,c^{(3)} \\
&\quad - (0.037 - 0.0031i)\,c^{(1)}\cos(3\phi) \\
&\quad - (0.0028 + 0.0378i)\,c^{(1)}\sin(3\phi)|^2, \\
I_{RP}(2\omega) &= B\,|(-0.0012 - 0.0034i)\,c^{(3)} \\
&\quad - (0.032 - 0.010i)\,c^{(2)} \\
&\quad - (0.00026 - 0.0012i)\,c^{(4)} \\
&\quad + (0.0031 - 0.049i)\,c^{(1)}\cos(3\phi) \\
&\quad - (0.047 + 0.0025i)\,c^{(1)}\sin(3\phi)|^2, \\
I_{LP}(2\omega) &= B\,|(-0.0012 - 0.0034i)\,c^{(3)} \\
&\quad - (0.032 - 0.010i)\,c^{(2)} \\
&\quad - (0.00026 - 0.0012i)\,c^{(4)} \\
&\quad + (0.0031 - 0.049i)\,c^{(1)}\cos(3\phi) \\
&\quad + (0.047 + 0.0025i)\,c^{(1)}\sin(3\phi)|^2,
\end{aligned} \tag{8}$$

where the subscripts for each $I_{\text{in-out}}(2\omega)$ refer to the input fundamental and output second harmonic polarizations, and $B = A \times I(\omega)^2$. In the above equations, $c^{(n)} = a^{(n)} + b^{(n)}$, where

$$\begin{aligned}
a^{(1)} &= \chi_{xxx}, \\
a^{(2)} &= \chi_{zxx}, \\
a^{(3)} &= 2\,\chi_{xxz}, \\
a^{(4)} &= \chi_{zzz}
\end{aligned} \tag{9}$$

represent the surface $\chi^{(2)}$ SHG and

$$\begin{aligned}
b^{(1)} &= -\chi_{xyyz}\mathcal{E}_z, \\
b^{(2)} &= \chi_{zxxz}\mathcal{E}_z, \\
b^{(3)} &= (\chi_{xzxz} + \chi_{xxzz})\mathcal{E}_z, \\
b^{(4)} &= \chi_{zzzz}\mathcal{E}_z
\end{aligned} \tag{10}$$

represent the electric-field-induced SHG over the accumulation region due to $\chi^{(3)}\vec{\mathcal{E}}$. The relative magnitudes of $c^{(n)}$ can be experimentally determined by measuring $I(2\omega)$ as a function of in-plane crystal orientation angle ϕ and laser polarization. The relative contributions of $a^{(n)}$ and $b^{(n)}$ can then be determined by varying the surface carrier density. The experimental results are reported in Sec. III.

III. EXPERIMENTAL RESULTS AND DISCUSSION

This section is organized into five parts. In Sec. III A we report our Bi_2Se_3 growth procedure, sample characterization results, and describe the optical techniques used to isolate second harmonic light. In Sec. III B we characterize the first-order linear optical response of our Bi_2Se_3 material, then the second-order nonlinear optical response in Sec. III C. In Sec. III D we report how changing the surface carrier concentration through molecular doping affects the SHG signal. Finally, in Sec. III E we characterize the intrinsic SHG CD from Bi_2Se_3.

A. Methods and sample characterization

In this work, samples of Bi_2Se_3 were lightly hole-doped by substituting As into the Se planes to reduce the bulk carrier concentration,[19,41] although they remain electrically conducting. Single-crystal $Bi_{2-x}As_xSe_3$ was grown by melting a 10-g stoichiometric mixture of Bi and Se shot with trace amounts of As powder ($x = 0.00129$) in an evacuated quartz tube at 850° C. After 12 h at this temperature, the mixture was cooled to 720° C over 2 hr, then slowly cooled to 650° C over 2 days. The batch was annealed at 650° C for 2 more days then furnace-cooled to room temperature.

After growth, the crystal orientation was determined by x-ray diffraction using a Bruker D8 diffractometer with CuKα radiation ($\lambda = 1.54$ Å) and a two-dimensional area detector. The real (n) and imaginary (k) parts of the index of refraction were determined between 350 and 820 nm by performing spectroscopic ellipsometry measurements using a Sopra GES 5 Spectroscopic Ellipsometer and accompanying WinElli software [Fig. 4(a)]. The optical penetration depth, which is given by $\xi = \lambda/4\pi k$[42], is shown in Fig. 4(b). We find that $\xi \sim 25$ nm at $\lambda = 795$ nm, which is the fundamental wavelength

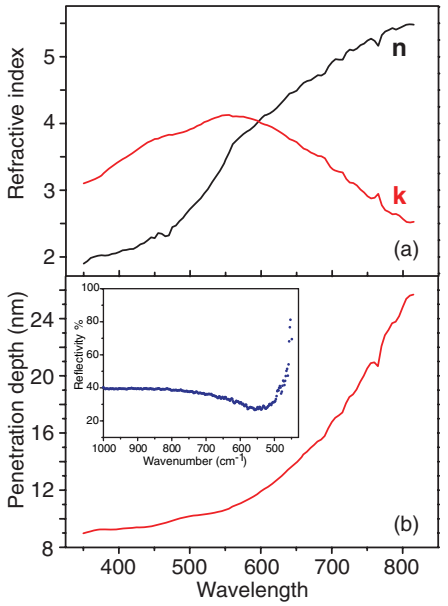

FIG. 4. (Color online) (a) Real and imaginary parts of the Bi_2Se_3 index of refraction as a function of light wavelength acquired by performing spectroscopic ellipsometry measurements. (b) Optical penetration depth as a function of wavelength. Inset: Measured FTIR reflectivity as a function of wave number normalized to the reflectivity of gold.

used in all SHG measurements. Samples were characterized by Fourier transform infrared spectroscopy (FTIR) using a Nicolet Magna 860 FTIR spectrometer [Fig. 4(b), inset]. The reflectivity minimum at $k \sim 557$ cm^{-3} ($f_p = 1.67 \times 10^{13}$ Hz) is due to resonant absorption at the plasma frequency. From this we calculate a bulk carrier density of $n = 3.68 \times 10^{17}$ cm^{-3} using the standard formula $\omega_p^2 = ne^2/\epsilon m^*$[41], where $\omega_p = 2\pi f_p$, e is the electron charge, $\epsilon(\omega_p) = 30\epsilon_0$ is the reported electric permittivity at the plasma frequency,[41] ϵ_0 is the permittivity of free space, and $m^* \sim 0.14m_e$[43] is the average effective mass of the bulk conduction band.

The SHG experimental layout is shown schematically in Fig. 5. Ultrashort laser pulses with a center wavelength of 795 nm ($\hbar\omega = 1.56$ eV) and a duration of 80 fs at FWHM were generated from a Ti:sapphire oscillator. The 80-MHz repetition rate was reduced to 1.6 MHz by a pulse picker and the average laser intensity of 0.63 kW/cm^2 used for the experiments is well below the experimentally determined Bi_2Se_3 damage threshold. The incident laser polarization was set by adjusting a $\lambda/2$ and a $\lambda/4$ wave plate. The beam was focused to a 20 μm $1/e^2$ spot size on the sample at an incident angle of 45°. Specularly reflected photons at the second harmonic energy ($\hbar 2\omega = 3.12$ eV) with polarization in (P) and out of (S) the scattering plane were spatially separated by a polarizing beam splitting cube and simultaneously measured using calibrated photomultiplier tubes sensitive to 3.1-eV photons. Before the photomultiplier tubes, the reflected fundamental light was removed through both absorptive and interference filtering. The second harmonic nature of the detected signal was confirmed by checking that it scaled quadratically with the incident beam intensity (Fig. 5, inset). Part of the incident beam was split off before the sample and passed through a β-barium

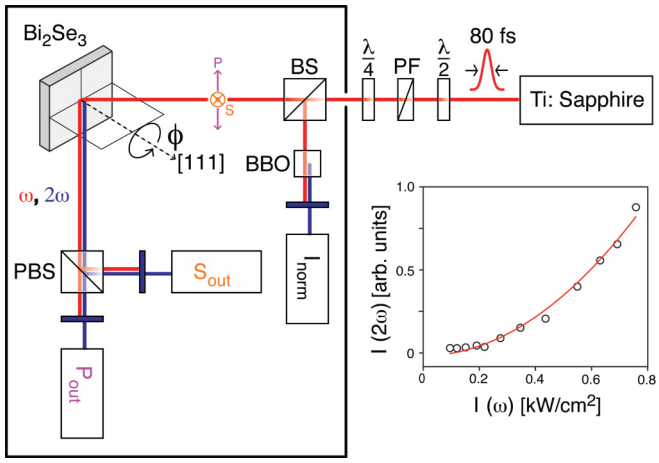

FIG. 5. (Color online) Schematic of the experimental layout showing the complete beam path. The paths of the fundamental (ω) and second harmonic (2ω) beams are shown in red and blue, respectively. Experiments were performed in a dark enclosure to avoid stray light (see contour). Optical elements are denoted as follows: polarizing beam splitter (PBS), quarter- and half-wave plate ($\lambda/4$ and $\lambda/2$), beam splitter (BS), polarization filter (PF), and β-barium borate (BBO). Photomultiplier tubes are shown as rectangles that measure the outgoing SHG, with P_{out} and S_{out} polarizations as labeled. The photomultiplier tube used to measure laser intensity fluctuations is labeled I_{norm}. Wavelength filters are shown as flat blue strips. Inset: Measured SHG intensity at $\phi = 0$ in the P_{in}-P_{out} polarization geometry as a function of the fundamental light intensity. The red line is a fit that shows the expected quadratic relationship between the two.

borate crystal to generate second harmonic light against which both P and S channels were normalized to account for laser intensity fluctuations. Bi_2Se_3(111) samples were mounted on a rotation stage and aligned so that the center of rotation coincided with the center of the focus of the incident beam. An accurate alignment was achieved by imaging the sample

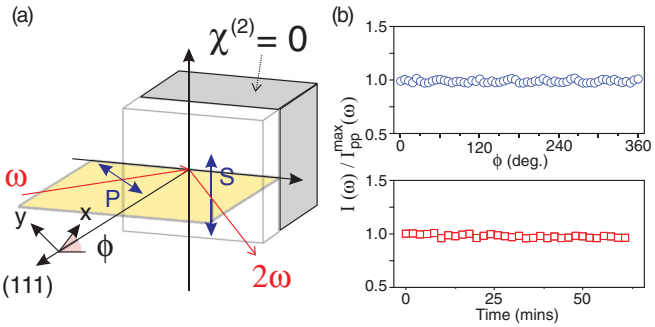

FIG. 6. (Color online) (a) Schematic of the SHG experimental geometry. Surface and bulk regions are shown in white and gray, respectively (panel reprinted from Ref. 29). (b) Top: Normalized intensity of the reflected beam at the fundamental frequency $I(\omega)$ from the (111) surface of Bi_2Se_3 measured as a function of azimuthal angle ϕ. Data are shown in the P_{in}-P_{out} polarization geometry, but similar isotropic patterns were obtained under all four linear and four circular polarization geometries. Bottom: Intensity $I(\omega)$ at $\phi = 0°$ in the P_{in}-P_{out} polarization geometry measured as a function of time after cleavage in air.

with a 50× microscope objective and a high-resolution CCD camera. The second harmonic light generated as a function of the in-plane crystal orientation was measured by recording $I(2\omega)$ in both polarization channels as a function of the sample rotation angle ϕ around the (111) axis and as a function of the incident polarization [Fig. 6(a)]. All samples were cleaved along the (111) plane in air or O_2 at room temperature prior to measurement. For the O_2 measurements, a continuous flow of O_2 (99.5% Airgas) gas was directed on the sample at a pressure of 10 psi and at a distance of approximately 1 cm inside a sealed enclosure.

B. First-order linear optical response

Before performing SHG measurements, we characterized the $\chi^{(1)}$ first-order linear optical response by measuring the reflected light intensity at the fundamental frequency of 200 min after the sample was cleaved in air. A typical trace is shown in the top panel of Fig. 6(b) for the P_{in}-P_{out} geometry. As a function of the sample rotation angle ϕ, $I(\omega)$ is clearly isotropic, confirming that all off-diagonal tensor elements of $\chi^{(1)}$ are 0 and that $\chi^{(1)}_{11} = \chi^{(1)}_{22}$ as expected from Eq. (3). Similar isotropic traces were recorded for all input-output polarization geometries.

In Sec. III C we show that $I(2\omega)$ increases after cleaving in air on the hour time scale before saturating. To check that this is not related to a change in the bulk electronic structure or bulk doping, we measured the time dependence of $I(\omega)$ immediately after cleaving in the P_{in}-P_{out} geometry, since the linear response is predominantly representative of bulk properties. It is clear from the bottom panel in Fig. 6(b) that after cleaving, the intensity of $I(\omega)$ remains constant out to at least 60 min. No measurable changes in $I(\omega)$ with time were observed at any ϕ or at any input-output polarization geometries.

C. Second-order nonlinear optical response

We now move on to characterize the second-order nonlinear optical response by measuring the second harmonic light generated from Bi_2Se_3(111). Equations (7) and (8) show that the tensor components of the combined $\chi^{(2)} + \chi^{(3)}\mathcal{E}$ susceptibilities, which encode the surface plus the accumulation-region electrical responses, respectively, can be determined by measuring $I(2\omega)$ as a function of the sample rotation angle ϕ in different input-output light polarization geometries. Figures 7(a)–7(d) show the results of these measurements taken with linearly polarized light 200 min after the sample was cleaved in air. Unlike the first-order optical response [Fig. 6(b)], $I(2\omega)$ is clearly anisotropic as a function of ϕ in all four linear polarization geometries. A simultaneous fit of Eqs. (7) and (8) to the SHG patterns (including those taken with circularly polarized light in Fig. 10) using a single set of susceptibility tensor elements yields excellent agreement [Figs. 7(a)–7(d)], which shows that the data are consistent with surface plus accumulation-layer SHG from Bi_2Se_3. From the fit results we determine the relative magnitudes of $|c^{(n)}|$:

$$|c^{(1)}| = 1,$$
$$|c^{(2)}| = 1.31,$$

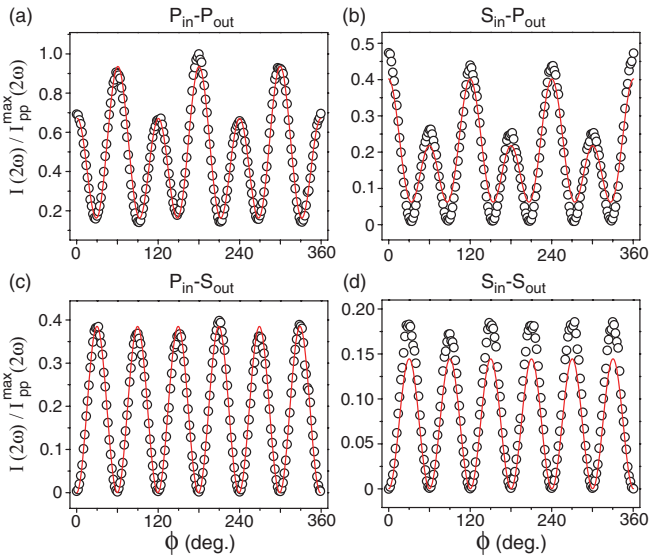

FIG. 7. (Color online) Normalized SHG intensity $I(2\omega)$ from the Bi_2Se_3(111) surface measured as a function of azimuthal angle ϕ between the bisectrix ($11\bar{2}$) and the scattering plane. Measurements taken 200 min after cleavage in (a) P_{in}-P_{out}, (b) S_{in}-P_{out}, (c) P_{in}-S_{out}, and (d) S_{in}-S_{out} incident and outgoing photon polarization geometries. All data sets are normalized to the maximum intensity measured at $t = 200$ min in the P_{in}-P_{out} geometry. Solid lines are fits to Eq. (7).

$$|c^{(3)}| = 0.19,$$
$$|c^{(4)}| = 8.99, \qquad (11)$$

where each $|c^{(n)}|$ is normalized to $|c^{(1)}|$. Because the phase of the complex fit parameters cannot be uniquely determined, it is only informative to show the absolute values. We find that the largest contribution to the combined $\chi^{(2)} + \chi^{(3)}\mathcal{E}$ nonlinear susceptibility comes from $|c^{(4)}|$, which describes the only purely out–of-plane electrical response at the surface [Eqs. (9) and (10)]. In Sec. III D we show that the relative contributions of surface ($\chi^{(2)}$) and accumulation-region ($\chi^{(3)}\mathcal{E}$) SHG can be determined by studying the time evolution of $I(2\omega)$ after cleaving the sample.

The data in Fig. 7 exhibit a clear three- or sixfold rotational symmetry, depending on whether the outgoing photons measured have a polarization component perpendicular (P polarized) or parallel (S polarized) to the sample plane, respectively. Because S-polarized light has only in-plane electric-field components, it is primarily a sensitive measure of the in-plane response. This likely originates from the anharmonic polarizability of the Se-Se bonds (Fig. 1), which have a sixfold symmetric arrangement in the sample plane. On the other hand, because P-polarized light contains an electric-field component along $\hat{z}$, it is sensitive to the out-of-plane response originating from the Se-Bi bonds, which have a threefold symmetric arrangement that extends into the bulk.

D. Surface molecular doping effects on SHG

To prove that the surface and accumulation-region SHG is dominant over multipole bulk effects, and to quantify their relative contributions, we studied the effects of changing the

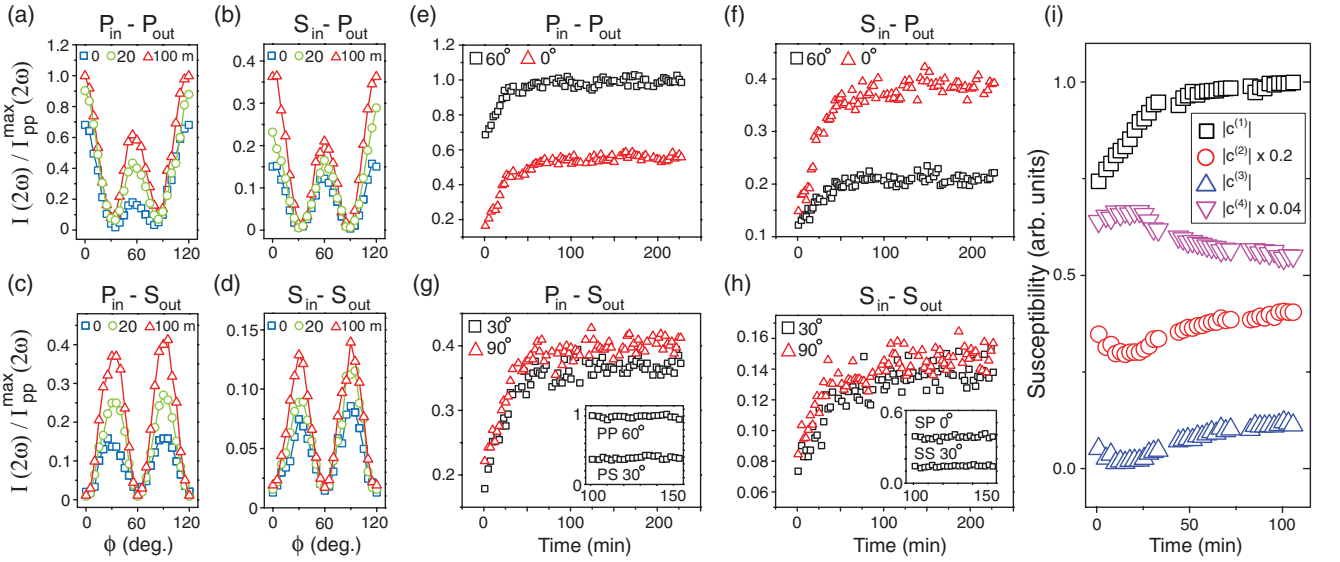

FIG. 8. (Color online) ϕ dependence of the normalized SHG intensity as a function of time after cleavage in air in the (a) P_{in}-P_{out}, (b) S_{in}-P_{out}, (c) P_{in}-S_{out}, and (d) S_{in}-S_{out} photon polarization geometries. (e–h) Accompanying detailed time dependence along high crystal symmetry directions (panels reprinted from Ref. 29). Insets in (g) and (h) show the time evolution of the peak SHG intensities starting at 100 min after cleavage in air, prior to which the sample was not exposed to laser light. (i) Fit coefficients from fitting Eq. (7) to the SHG data as a function of time after cleavage in air. The gaps in the data at approximately 5, 40, and 75 min are where full $\phi = 0^\circ$ to $\phi = 360^\circ$ traces were taken to confirm that rotational symmetry was maintained as a function of time.

surface carrier concentration. Angle-resolved photoemission spectroscopy (ARPES) studies have shown that Bi_2Se_3 exhibits an intrinsic surface band bending after cleavage in ultrahigh vacuum (UHV) that acts to monotonically increase the electron density at the surface on the hour time scale until a stable accumulation layer is formed.[8,17,44] If SHG from Bi_2Se_3 is in fact surface sensitive, such a surface electronic change should be manifested in our measurements. This is because, as shown in Sec. II A, the band-bending-induced electric field acts to break inversion symmetry over the depth to which it penetrates into the bulk (Fig. 2), thereby permitting SHG in the accumulation region with an intensity that is proportional to the field strength. Figures 8(a)–8(d) show a clear increase in $I(2\omega)$ at all ϕ and in all input-output linear polarization geometries as a function of time after cleavage in air. However, there is no change in the rotational symmetry of the SHG patterns, which rules out any trigonal symmetry-breaking atomic reconstruction, as is typical of semiconductors such as Si(111) in air.[31] Figures 8(e)–8(h) show the complete time dependencies of the SHG peak intensities, which all undergo the same monotonic increase by as much as 400% within 50 min following cleavage, after which they saturate to a value that remains constant out to at least 600 min. This is a trend highly consistent with the time evolution of the surface Fermi level observed using ARPES[8] and cannot have a bulk origin as no bulk electronic changes were observed with time after cleaving [Fig. 6(b)].

Slow photoinduced changes in SHG intensity are known to occur on semiconductor surfaces such as GaAs[45] and oxidized Si[34,46] through a two-step charge-excitation charge-trapping processes.[34,45] To test for such effects, we repeated the measurements after keeping the sample unexposed to laser light for the first 100 min after cleavage [Figs. 8(g) and 8(h), insets]. The fact that the SHG intensities under these conditions show no time dependence and match the previous saturation intensities shows that the observed time evolution is purely a surface doping effect and not a photoinduced effect.

To understand how the nonlinear susceptibilities evolve with time, we simultaneously fit the SHG data in Figs. 8(e)–8(h) at each point in time to Eq. (7). The time dependence of the fit coefficients is shown in Fig. 8(i). We find that $|c^{(1)}|$, $|c^{(2)}|$, and $|c^{(3)}|$, which together primarily encode the in-plane electrical response [Eqs. (9) and (10)], generally increase as a function of time. This precludes a change in the interatomic-layer distance at the surface after cleaving as the primary source of the increased SHG signal because this would predominantly affect only the out-of-plane susceptibilities. The coefficient $|c^{(4)}|$, which describes the only purely out-of-plane electrical response, on the other hand, generally decreases as a function of time. The dip feature exhibited by $|c^{(2)}|$, $|c^{(3)}|$, and $|c^{(4)}|$ at early times is currently unclear and requires and awaits a detailed microscopic theoretical description of SHG from Bi_2Se_3. However, we note that this feature is similar to that observed in the raw SHG data for samples cleaved in an O_2 environment as a function of time in Figs. 9(a) and 9(b).

Because we find that the band bending in air occurs on the same time scale observed in samples cleaved in UHV, its cause is unlikely related to the direct charging of the surface by adsorbed molecules from the environment, as the adsorption rates in air and UHV will be different by orders of magnitude. An alternative possibility is that it is due to an intrinsic material property. Intrinsic band bending is known to occur through the migration of charged impurities within the crystal—a process that can take place on the hour time scale.[47] If this is the case in our samples, the migrating impurities are most likely

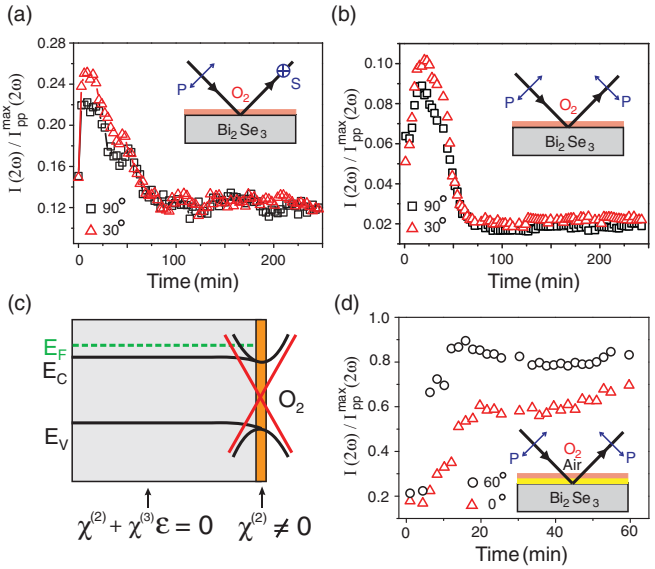

FIG. 9. (Color online) (a) Time dependence of SHG peak intensities measured in the P_{in}-S_{out} polarization geometry after cleaving in O_2 (panel reprinted from Ref. 29). (b) Time dependence of SHG minima measured in the P_{in}-P_{out} polarization geometry after cleaving in O_2. Similar behaviors were also observed in other polarization geometries. (c) Schematic of the energy evolution of the bulk conduction band minimum (E_C) and bulk valence band maximum (E_V) relative to the Fermi level (E_F) as a function of distance to the O_2 covered surface. (d) Time dependence of the SHG peak intensities measured in the P_{in}-P_{out} polarization geometry after cleaving in air, then immediately covering the surface with O_2 gas.

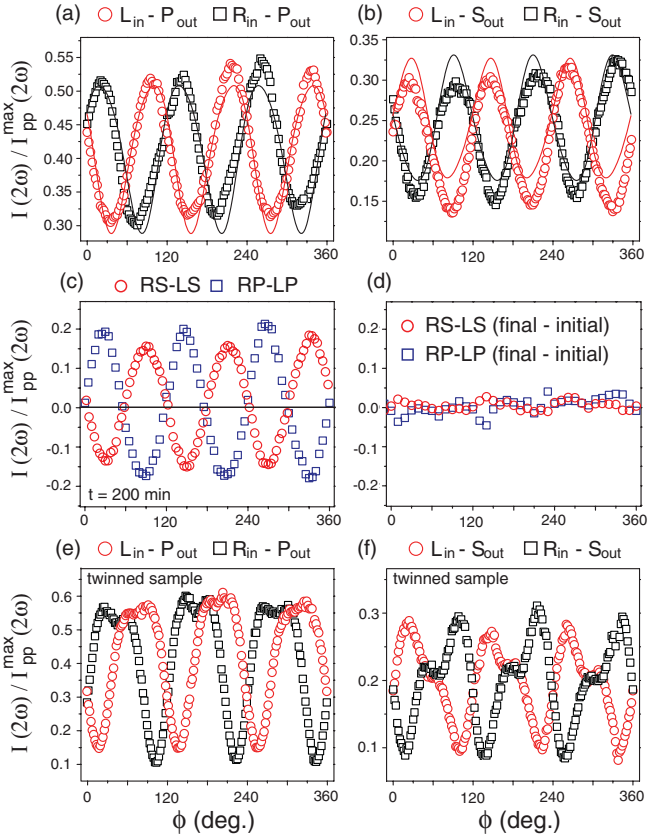

FIG. 10. (Color online) Normalized ϕ-dependent SHG intensity patterns from Bi_2Se_3 measured 200 min after cleavage in air under (a) left-circular in (L_{in}) P_{out} and right-circular in (R_{in}) P_{out} and (b) L_{in}-S_{out} and R_{in}-S_{out} photon polarization geometries. Solid lines are theoretical fits to Eq. (8). (c) Circular dichroism ($I_R - I_L$) corresponding to data in (a) and (b). (d) Difference between circular dichroism measured at 200 min after cleavage and that measured immediately after cleavage [(c) and (d) reprinted from Ref. 29]. Normalized SHG intensity patterns from a different sample batch that are likely crystal twinned in (e) left-circular in (L_{in}) P_{out} and right-circular in (R_{in}) P_{out} and (f) L_{in}-S_{out} and R_{in}-S_{out} photon polarization geometries.

negatively charged Se vacancies; they are prolific in Bi_2Se_3,[41] which may move to the surface to lower the surface energy of the topmost Se layer after cleaving, thereby increasing the surface carrier density.

Although we have shown that the $\chi^{(2)}$ and $\chi^{(3)}\mathcal{E}$ contributions to SHG from Bi_2Se_3(111) can be distinguished, isolating the surface electrical response, which is only encoded in $\chi^{(2)}$, will require eliminating the accumulation-region SHG. Experiments have shown that O_2 is an effective electron acceptor when deposited on the surface of Bi_2Se_3.[48] To demonstrate that the accumulation-region SHG can be eliminated and to confirm that SHG is sensitive to tuning of the surface carrier density, we studied the time evolution of $I(2\omega)$ after cleaving the sample in an O_2 environment. Figures 9(a) and 9(b) show that $I(2\omega)$ initially increases, to reach approximately 50% of the saturation intensity value in air, then slowly decreases back to its initial value. These results show that electron transfer from the Bi_2Se_3 surface to the adsorbed O_2 molecules takes place only after some finite surface charge has developed and that O_2 can restore the surface back to an uncharged state, where $\vec{\mathcal{E}} = 0$, but cannot hole dope beyond this state [Fig. 9(c)]. Figure 9(d) shows that this hole doping does not occur when the sample is cleaved in air, then immediately exposed to O_2, indicating that the charge transfer only occurs by molecules initially adsorbed on the surface.

Assuming that the surface doping is negligibly small immediately after cleaving in air ($\vec{\mathcal{E}} \sim 0$), we estimate that the $\chi^{(2)}$ and $\chi^{(3)}\mathcal{E}$ contributions to SHG are roughly equal at long times after cleaving in air. We estimate that the accumulation region penetrates approximately 12 nm into the bulk using the Thomas-Fermi screening length $\lambda_{TF} = (3ne^2/2\epsilon_{dc}E_f)^{-1/2}$[49] as an approximation, where $n = 3.68 \times 10^{17}$ cm^{-3} is the bulk carrier density [Fig. 4(b) inset], $\epsilon_{dc} \sim 113\epsilon_0$ is the dc electric permitivity for Bi_2Se_3,[43] and we approximate $E_f = \frac{\hbar^2}{2m^*}(3\pi^2 n)^{2/3} = 0.013$ eV using $m^* = 0.14m_e$.[43]

E. Circular dichroism SHG

Having established that a pure surface $\chi^{(2)}$ measurement can be performed on the Bi_2Se_3 materials class that is sensitive to both the surface crystal structure and the surface carrier concentration, we consider how SHG can be used to monitor time-reversal symmetry (TRS) at a topological insulator surface. It has been proposed that new TRS broken phases can be measured through the differential absorption of right (R) versus left (L) circularly polarized light.[14,22,23] In order to understand

whether second harmonic versions of such experiments are feasible, it is necessary to measure the intrinsic second-order optical response of Bi_2Se_3 to circular-polarized light.

Second harmonic CD, the difference in SHG yield using incident R- versus L-circularly polarized fundamental light, was measured from Bi_2Se_3 200 min after cleavage in air. Figures 10(a) and 10(b) show a clear difference in the SHG intensity patterns measured using R- versus L-circularly polarized input for both S- and P-polarized output geometries, which are well described by Eq. (8) using the same set of susceptibility values fitted to Figs. 7(a)–7(d). By plotting CD as a function of ϕ [Fig. 10(c)], we find that CD varies sinusoidally, with the S- and P-polarized output components out of phase by exactly 180°. Although second harmonic CD can arise through the interference of higher-order bulk multipole and surface dipole SHG radiation, such effects are known to be suppressed when the photon energy exceeds the bulk band gap,[35] and we have shown that the bulk multipole contributions to SHG are negligible. Equation (8) shows that that CD SHG can be generated by the surface alone.

While CD is generally nonzero, Fig. 10(c) shows that it vanishes when ϕ is an integer multiple of 60°, angles where the scattering plane coincides with a mirror plane of the (111) surface (Fig. 1). Such zeros are protected by mirror symmetry because R- and L-circularly polarized light transform into one another under mirror reflection about the scattering plane. Because a magnetization can break mirror symmetry, measuring departures from 0 in CD along these specific values of ϕ can be a sensitive probe of TRS breaking on the surface of Bi_2Se_3. Remarkably, we find that CD at a general ϕ is insensitive to surface charging, as evidenced by the lack of measurable change as a function of time after cleavage [Fig. 10(d)]. This suggests that sensitive searches for TRS-breaking-induced CD may be carried out without the need for careful control of surface charging, which is an important and robust way to study the physics of surface-doped topological insulators or buried interfaces between topological insulators and ordinary materials.[1,2] We are currently investigating why CD is insensitive to surface charging.

In certain samples, the ϕ dependence of $I(2\omega)$ with circularly polarized light exhibited additional features that cannot be accounted for by Eq. (8) [Figs. 10(e) and 10(f)]. These appear to be smaller SHG extrema that are shifted from the extrema exhibited in Figs. 10(a) and 10(b) by 60°. However, the ϕ dependence of $I(2\omega)$ in the linear polarization input configurations in the same samples appeared to be unaffected due to the 60° periodicity of the SHG extrema. The origin of these features is likely due to crystal twinning, and further confirmation is under way.

IV. SUMMARY AND OUTLOOK

We have presented a theoretical and experimental study of SHG from the topological insulator Bi_2Se_3. By performing a crystal symmetry analysis we identified the nonlinear electric susceptibility tensor elements that contribute to SHG. The analysis showed that the process is forbidden in the bulk of Bi_2Se_3, owing to the presence of inversion symmetry, but can be generated at the surface, where inversion symmetry is necessarily broken. We also found that SHG can be generated near the surface in the accumulation region, where the band-bending electric field breaks inversion symmetry over the depth to which it penetrates into the bulk. We incorporated the symmetry analysis results into a phenomenological model and showed that the relative magnitudes of the susceptibility tensor elements can be determined by measuring the SHG intensity and polarization as a function of the in-plane crystal orientation and incident laser polarization.

To test the model, we performed SHG experiments on bulk single crystals of Bi_2Se_3. We first described the sample growth process and reported the characterization results. We also determined the complex index of refraction in the visible range, which is a necessary input parameter to the theoretical model, by performing spectroscopic ellipsometry measurements. We described the experiment we designed to isolate the SHG signal and characterized the first-order linear optical response. We measured the radiated SHG intensity and polarization as a function of crystal orientation and incident laser polarization, and the results are consistent with our theoretical model. We fit the data and reported the relative contributions to SHG from each of the nonlinear susceptibility elements.

To confirm that the surface and accumulation region are the dominant source of SHG and to quantify their relative contributions, we performed a surface-doping dependence study. When the sample was cleaved in air, the SHG intensity in all polarization configurations monotonically increased on the hour time scale before saturating and remaining constant out to at least several hours. We attributed this behavior to the slow formation of the SHG generating accumulation region that results from the intrinsic band bending in Bi_2Se_3 after cleaving.[8,17] We estimated from the results that the surface and accumulation-region contributions to SHG were comparable at long times in air. When cleaved in an oxygen environment, the SHG intensity initially increased, then slowly decreased back to its initial value. This is consistent with ARPES results showing that depositing oxygen on the surface of Bi_2Se_3 lowers the surface carrier density and hence the magnitude of the band-bending electric field that induces SHG in the accumulation region.[48] These results show that SHG can be used to monitor changes in the surface Fermi level.

We finally investigated the SHG response using circularly polarized light as a function of the in-plane crystal orientation. We found pronounced CD at all crystal rotation angles except along planes of crystal mirror symmetry, where the CD vanished. We proposed that sensitive searches for TRS breaking could be performed by monitoring the SHG CD along these mirror planes.

The theoretical description and experimental realization of surface SHG from the Bi_2Se_3 materials class provide a novel contact-free probe of the electrical response from a single surface of a topological insulator. The ability to perform such surface-sensitive experiments with tuning control of the surface carrier concentration under ambient conditions is promising for future technological applications of topological insulators.

ACKNOWLEDGMENT

This work is supported by D.O.E. Grant No. DE-FG02-08ER46521.

APPENDIX

1. Symmetry analysis of tensor components

Similarly to the procedure used to find the $\chi^{(1)}$ components, the nonvanishing $\chi^{(2)}$ tensor elements can be found by transforming $\chi^{(2)}$ under the C_{3v} rotation and mirror symmetry operations (Fig. 1) via Eq. (2) and equating the resulting tensors. We find that $\chi^{(2)}$ assumes the form[31]

$$\chi^{(2)} = \begin{pmatrix} \begin{pmatrix} \chi_{xxx} \\ 0 \\ \chi_{xxz} \end{pmatrix} & \begin{pmatrix} 0 \\ -\chi_{xxx} \\ 0 \end{pmatrix} & \begin{pmatrix} \chi_{xxz} \\ 0 \\ 0 \end{pmatrix} \\ \begin{pmatrix} 0 \\ -\chi_{xxx} \\ 0 \end{pmatrix} & \begin{pmatrix} -\chi_{xxx} \\ 0 \\ \chi_{xxz} \end{pmatrix} & \begin{pmatrix} 0 \\ \chi_{xxz} \\ 0 \end{pmatrix} \\ \begin{pmatrix} \chi_{zxx} \\ 0 \\ 0 \end{pmatrix} & \begin{pmatrix} 0 \\ \chi_{zxx} \\ 0 \end{pmatrix} & \begin{pmatrix} 0 \\ 0 \\ \chi_{zzz} \end{pmatrix} \end{pmatrix},$$

which contains four nonzero independent components: χ_{xxx} ($=-\chi_{xyy} = -\chi_{yxy}$), χ_{zxx} ($=\chi_{zyy}$), χ_{xxz} ($=\chi_{yyz}$), and χ_{zzz}, and x, y, and z refer to the crystal coordinates defined in Fig. 1. Here we choose the tensor representation, where the index i represents the row, j the column, and k the row within each ij element. Since we perform experiments by rotating a sample about its (111) axis, we transform $\chi^{(2)}$ from the sample coordinate frame to the laboratory coordinate frame using Eq. (2) with T substituted by the rotation matrix[31]

$$R(\phi) = \begin{pmatrix} \cos(\phi) & -\sin(\phi) & 0 \\ \sin(\phi) & \cos(\phi) & 0 \\ 0 & 0 & 1 \end{pmatrix}.$$

This yields[31]

$$\chi^{(2)} \rightarrow \begin{pmatrix} \begin{pmatrix} \chi_{xxx}\cos(3\phi) \\ -\chi_{xxx}\sin(3\phi) \\ \chi_{xxz} \end{pmatrix} & \begin{pmatrix} -\chi_{xxx}\sin(3\phi) \\ -\chi_{xxx}\cos(3\phi) \\ 0 \end{pmatrix} & \begin{pmatrix} \chi_{xxz} \\ 0 \\ 0 \end{pmatrix} \\ \begin{pmatrix} -\chi_{xxx}\sin(3\phi) \\ -\chi_{xxx}\cos(3\phi) \\ 0 \end{pmatrix} & \begin{pmatrix} -\chi_{xxx}\cos(3\phi) \\ \chi_{xxx}\sin(3\phi) \\ \chi_{xxz} \end{pmatrix} & \begin{pmatrix} 0 \\ \chi_{xxz} \\ 0 \end{pmatrix} \\ \begin{pmatrix} \chi_{zxx} \\ 0 \\ 0 \end{pmatrix} & \begin{pmatrix} 0 \\ \chi_{zxx} \\ 0 \end{pmatrix} & \begin{pmatrix} 0 \\ 0 \\ \chi_{zzz} \end{pmatrix} \end{pmatrix}.$$

We now impose the same symmetry conditions on $\chi^{(3)}$ as done above for $\chi^{(2)}$. Unlike odd-rank tensors, all components of even-rank tensors do not necessarily vanish under inversion symmetry. Therefore, the $\chi^{(3)}$ contribution to SHG does not necessarily vanish in the bulk. However, SHG will only be generated by $\chi^{(3)}$ over the finite accumulation region that the band-bending field $\vec{\mathcal{E}}$ penetrates into the bulk. In general, $\chi^{(3)}$ has 81 components. Under the transformations by the symmetry operations of D_{3d}^5, this is reduced to the form

$$\chi^{(3)} = \begin{pmatrix} \chi_{11}^{(3)} & \chi_{12}^{(3)} & \chi_{13}^{(3)} \\ \chi_{21}^{(3)} & \chi_{22}^{(3)} & \chi_{23}^{(3)} \\ \chi_{31}^{(3)} & \chi_{32}^{(3)} & \chi_{33}^{(3)} \end{pmatrix},$$

where[51]

$$\chi_{11}^{(3)} = \begin{pmatrix} \chi_{xxxx} & 0 & -\chi_{xyyz} \\ 0 & \chi_{xxyy} & 0 \\ -\chi_{xyzy} & 0 & \chi_{xxzz} \end{pmatrix},$$

$$\chi_{12}^{(3)} = \begin{pmatrix} 0 & \chi_{xyxy} & 0 \\ \chi_{xxxx} - \chi_{xxyy} - \chi_{xyxy} & 0 & \chi_{xyyz} \\ 0 & \chi_{xyzy} & 0 \end{pmatrix},$$

$$\chi_{13}^{(3)} = \begin{pmatrix} -\chi_{xzyy} & 0 & \chi_{xzxz} \\ 0 & \chi_{xzyy} & 0 \\ \chi_{xzzx} & 0 & 0 \end{pmatrix},$$

$$\chi_{21}^{(3)} = \begin{pmatrix} 0 & \chi_{xxxx} - \chi_{xxyy} - \chi_{xyxy} & 0 \\ \chi_{xyxy} & 0 & \chi_{xyyz} \\ 0 & \chi_{xyzy} & 0 \end{pmatrix},$$

$$\chi_{22}^{(3)} = \begin{pmatrix} \chi_{xxyy} & 0 & \chi_{xyyz} \\ 0 & \chi_{xxxx} & 0 \\ \chi_{xyzy} & 0 & \chi_{xxzz} \end{pmatrix},$$

$$\chi_{23}^{(3)} = \begin{pmatrix} 0 & \chi_{xzyy} & 0 \\ \chi_{xzyy} & 0 & \chi_{xzxz} \\ 0 & \chi_{xzzx} & 0 \end{pmatrix},$$

$$\chi_{31}^{(3)} = \begin{pmatrix} -\chi_{zxyy} & 0 & \chi_{zxxz} \\ 0 & \chi_{zxyy} & 0 \\ \chi_{zxzx} & 0 & 0 \end{pmatrix},$$

$$\chi_{32}^{(3)} = \begin{pmatrix} 0 & \chi_{zxyy} & 0 \\ \chi_{zxyy} & 0 & \chi_{zxxz} \\ 0 & \chi_{zxzx} & 0 \end{pmatrix},$$

$$\chi_{33}^{(3)} = \begin{pmatrix} \chi_{zzxx} & 0 & 0 \\ 0 & \chi_{zzxx} & 0 \\ 0 & 0 & \chi_{zzzz} \end{pmatrix},$$

which contains 17 independent components.[50] In the laboratory coordinate frame, $\chi^{(3)}$ transforms according to[51]

$$\chi_{11}^{(3)} \rightarrow \begin{pmatrix} \chi_{xxxx} & 0 & -\chi_{xyyz}\cos(3\phi) \\ 0 & \chi_{xxyy} & -\chi_{xyyz}\sin(3\phi) \\ -\chi_{xyzy}\cos(3\phi) & -\chi_{xyzy}\sin(3\phi) & \chi_{xxzz} \end{pmatrix},$$

$$\chi_{12}^{(3)} \rightarrow \begin{pmatrix} 0 & \chi_{xyxy} & -\chi_{xyyz}\sin(3\phi) \\ \chi_{xxxx} - \chi_{xxyy} - \chi_{xyxy} & 0 & \chi_{xyyz}\cos(3\phi) \\ -\chi_{xyzy}\sin(3\phi) & \chi_{xyzy}\cos(3\phi) & 0 \end{pmatrix},$$

$$\chi^{(3)}_{13} \rightarrow \begin{pmatrix} -\chi_{xzyy}\cos(3\phi) & -\chi_{xzyy}\sin(3\phi) & \chi_{xzxz} \\ -\chi_{xzyy}\sin(3\phi) & \chi_{xzyy}\cos(3\phi) & 0 \\ \chi_{xzzx} & 0 & 0 \end{pmatrix},$$

$$\chi^{(3)}_{21} \rightarrow \begin{pmatrix} 0 & \chi_{xxxx} - \chi_{xxyy} - \chi_{xyxy} & -\chi_{xyyz}\sin(3\phi) \\ \chi_{xyxy} & 0 & \chi_{xyyz}\cos(3\phi) \\ -\chi_{xyzy}\sin(3\phi) & \chi_{xyzy}\cos(3\phi) & 0 \end{pmatrix},$$

$$\chi^{(3)}_{22} \rightarrow \begin{pmatrix} \chi_{xxyy} & 0 & \chi_{xyyz}\cos(3\phi) \\ 0 & \chi_{xxxx} & \chi_{xyyz}\sin(3\phi) \\ \chi_{xyzy}\cos(3\phi) & \chi_{xyzy}\sin(3\phi) & \chi_{xxzz} \end{pmatrix},$$

$$\chi^{(3)}_{23} \rightarrow \begin{pmatrix} -\chi_{xzyy}\sin(3\phi) & \chi_{xzyy}\cos(3\phi) & 0 \\ \chi_{xzyy}\cos(3\phi) & \chi_{xzyy}\sin(3\phi) & \chi_{xzxz} \\ 0 & \chi_{xzzx} & 0 \end{pmatrix},$$

$$\chi^{(3)}_{31} \rightarrow \begin{pmatrix} -\chi_{zxyy}\cos(3\phi) & -\chi_{zxyy}\sin(3\phi) & \chi_{zxxz} \\ -\chi_{zxyy}\sin(3\phi) & \chi_{zxyy}\cos(3\phi) & 0 \\ \chi_{zxzx} & 0 & 0 \end{pmatrix},$$

$$\chi^{(3)}_{32} \rightarrow \begin{pmatrix} -\chi_{zxyy}\sin(3\phi) & \chi_{zxyy}\cos(3\phi) & 0 \\ \chi_{zxyy}\cos(3\phi) & \chi_{zxyy}\sin(3\phi) & \chi_{zxxz} \\ 0 & \chi_{zxzx} & 0 \end{pmatrix},$$

$$\chi^{(3)}_{33} \rightarrow \begin{pmatrix} \chi_{zzxx} & 0 & 0 \\ 0 & \chi_{zzxx} & 0 \\ 0 & 0 & \chi_{zzzz} \end{pmatrix}.$$

*Correspondence author: gedik@mit.edu

[1] J. E. Moore, Nature **464**, 194 (2010).
[2] M. Z. Hasan and C, L. Kane, Rev. Mod. Phys. **82**, 3045 (2010).
[3] X.-L. Qi and S.-C. Zhang, Phys. Today **63**, 33 (2010).
[4] D. Hsieh *et al*., Nature **452**, 970 (2008).
[5] D. Hsieh *et al*., Science **323**, 919 (2009).
[6] Y. Xia *et al*., Nature Phys. **5**, 398 (2009).
[7] Y. L. Chen *et al*., Science **325**, 5937 (2009).
[8] D. Hsieh *et al*., Nature **460**, 1101 (2009).
[9] P. Roushan *et al*., Nature **460**, 1106 (2009).
[10] Z. Alpichshev, J. G. Analytis, J. H. Chu, I. R. Fisher, Y. L. Chen, Z. X. Shen, A. Fang, and A. Kapitulnik, Phys. Rev. Lett. **104**, 016401 (2010).
[11] S. Raghu, S. B. Chung, X.-L. Qi, and S.-C. Zhang, Phys. Rev. Lett. **104**, 116401 (2010).
[12] P. Hosur, Phys. Rev. B **83**, 035309 (2011).
[13] J. W. McIver, D. Hsieh, H. Steinberg, P. Jarillo-Herrero, and N. Gedik, Nature Nano. **7**, 96 (2012).
[14] X.-L. Qi, T. L. Hughes, and S.-C. Zhang, Phys. Rev. B **78**, 195424 (2008).
[15] G. Rosenberg and M. Franz, Phys. Rev. B **82**, 035105 (2010).
[16] H. Zhang *et al*., Nature Phys. **5**, 438 (2009).
[17] D. Hsieh *et al*., Phys. Rev. Lett. **103**, 146401 (2009).
[18] J. G. Checkelsky, Y. S. Hor, R. J. Cava, and N. P. Ong, Phys. Rev. Lett. **106**, 196801 (2011).
[19] H. Steinberg, D. R. Gardner, Y. S. Lee, and P. Jarillo-Herrero, Nano Lett. **10**, 5032 (2010).
[20] Y. S. Kim *et al*., Phys. Rev. B **84**, 073109 (2011).
[21] L. A. Wray *et al*., arXiv:1105.4794.
[22] W.-K. Tse and A. H. MacDonald, Phys. Rev. Lett. **105**, 057401 (2010).
[23] J. Maciejko, X.-L. Qi, H. D. Drew, and S.-C. Zhang, Phys. Rev. Lett. **105**, 166803 (2010).
[24] A. B. Sushkov, G. S. Jenkins, D. C. Schmadel, N. P. Butch, J. Paglione, and H. D. Drew, Phys. Rev. B **82**, 125110 (2010).
[25] A. D. LaForge, A. Frenzel, B. C. Pursley, T. Lin, X. Liu, J. Shi, and D. N. Basov, Phys. Rev. B **81**, 125120 (2010).
[26] N. P. Butch, K. Kirshenbaum, P. Syers, A. B. Sushkov, G. S. Jenkins, H. D. Drew, and J. Paglione, Phys. Rev. B **81**, 241301(R) (2010).
[27] J. N. Hancock, J. L. M. van Mechelen, A. B. Kuzmenko, D. van der Marel, C. Brune, E. G. Novik, G. V. Astakhov, H. Buhmann, and L. W. Molenkamp, Phys. Rev. Lett. **107**, 136803 (2011).
[28] R. Valdes Aguilar *et al*., arXiv:1105.0237.
[29] D. Hsieh, J. W. McIver, D. H. Torchinsky, D. R. Gardner, Y. S. Lee and N. Gedik, Phys. Rev. Lett. **106**, 057401 (2011).
[30] D. Hsieh, F. Mahmood, J. W. McIver, D. R. Gardner, Y. S. Lee, and N. Gedik, Phys. Rev. Lett. **107**, 077401 (2011).
[31] Y. R. Shen, in *The Principles of Nonlinear Optics*, (Wiley-Interscience, New York, 1984).
[32] R. R. Birss, *Symmetry and Magnetism* (North-Holland, Amsterdam, 1964).
[33] H. L. Dai and W. Ho, *Laser Spectroscopy and Photo-chemistry on Metal Surfaces* (World Scientific, Singapore, 1995).
[34] J. Bloch, J. G. Mihaychuk, and H. M. van Driel, Phys. Rev. Lett. **77**, 920 (1996).
[35] F.-X. Wang, F. J. Rodriguez, W. M. Albers, R. Ahorinta, J. E. Sipe, and M. Kauranen, Phys. Rev. B **80**, 233402 (2009).
[36] X. Li *et al*., Appl. Phys. Lett. **89**, 022102 (2009).
[37] V. Mizrahi and J. E. Sipe, J. Opt. Soc. Am. B **5**, 660 (1988).
[38] T. F. Heinz, Ph.D. thesis, University of California, Berkeley, 1982.
[39] N. Bloembergen and P. S. Pershan, Phys. Rev. **128**, 606 (1962).
[40] E. Hecht, *Optics*, 3rd ed. (Addison-Wesley, Boston, 1998), p. 111.
[41] A. Sklenar, C. Drasar, A. Krejcova, and P. Lostak, Cryst. Res. Technol. **35**, 1069 (2000).
[42] H. Fujiwara, *Spectrocopic Ellipsometry: Principles and Applications* (John Wiley & Sons, Chichester, UK, 2007), p. 23.
[43] J. G. Analytis, J. H. Chu, Y. Chen, F. Corredor, R. D. McDonald, Z. X. Shen, and I. R. Fisher, Phys. Rev. B **81**, 205407 (2010).
[44] M. Bianchi *et al*., Nature Commun. **1**, 128 (2010).
[45] J. Qi, M. S. Yeganeh, I. Koltover, A. G. Yodh, and W. M. Theis, Phys. Rev. Lett. **71**, 633 (1993).
[46] S. A. Mitchell, T. R. Ward, D. D. M. Wayner, and G. P. Lopinski, J. Phys. Chem. B **106**, 9873 (2002).
[47] A. Sosin, Phys. Rev. **122**, 1112 (1961).
[48] Y. L. Chen *et al*., Science **329**, 659 (2010).
[49] N. W. Ashcroft and N. D. Mermin, *Solid State Physics* (Thompson Learning, Tampa, FL, 1976), p. 342.
[50] S. V. Popov, Yu. P. Svirko, and N. I. Zheludev, *Susceptibility Tensors for Nonlinear Optics* (IOP, London, 1995).
[51] R. Boyd, *Nonlinear Optics*, 3rd ed. (Elsevier, New York, 2008).